

We are IntechOpen, the world's leading publisher of Open Access books Built by scientists, for scientists

6,900

Open access books available

186,000

International authors and editors

200M

Downloads

Our authors are among the

154

Countries delivered to

TOP 1%

most cited scientists

12.2%

Contributors from top 500 universities



WEB OF SCIENCE™

Selection of our books indexed in the Book Citation Index
in Web of Science™ Core Collection (BKCI)

Interested in publishing with us?
Contact book.department@intechopen.com

Numbers displayed above are based on latest data collected.
For more information visit www.intechopen.com



Dynamic Modeling and Power Modeling of Robotic Skid-Steered Wheeled Vehicles

Wei Yu, Emmanuel Collins and Oscar Chuy
Florida State University
U.S.A

1. Introduction

Dynamic models and power models of autonomous ground vehicles are needed to enable realistic motion planning Howard & Kelly (2007); Yu et al. (2010) in unstructured, outdoor environments that have substantial changes in elevation, consist of a variety of terrain surfaces, and/or require frequent accelerations and decelerations.

At least 4 different motion planning tasks can be accomplished using appropriate dynamic and power models:

1. *Time optimal motion planning.*
2. *Energy efficient motion planning.*
3. *Reduction in the frequency of replanning.*
4. *Planning in the presence of a fault, such as flat tire or faulty motor.*

For the purpose of motion planning this chapter focuses on developing dynamic and power models of a skid-steered wheeled vehicle to help the above motion planning tasks. The dynamic models are the foundation to derive the power models of skid-steered wheeled vehicles. The target research platform is a skid-steered vehicle. A skid-steered vehicle can be either tracked or wheeled. Fig. 1 shows examples of a skid-steered wheeled vehicle and a skid-steered tracked vehicle.

This chapter is organized into five sections. Section 1 is the introduction. Section 2 presents the kinematic models of a skid-steered wheeled vehicle, which is the preliminary knowledge to the proposed dynamic model and power model. Section 3 develops analytical dynamic models of a skid-steered wheeled vehicle for general 2D motion. The developed models are characterized by the coefficient of rolling resistance, the coefficient of friction, and the shear deformation modulus, which have terrain-dependent values. Section 4 develops analytical power models of a skid-steered vehicle and its inner and outer motors in general 2D curvilinear motion. The developed power model builds upon a previously developed dynamic model in Section 3. Section 5 experimentally verifies the proposed dynamic models and power models of a robotic skid-steered wheeled vehicle.

Ackerman steering, differential steering, and skid steering are the most widely used steering mechanisms for wheeled and tracked vehicles. Ackerman steering has the advantages of good lateral stability when turning at high speeds, good controllability Siegwart & Nourbakhsh (2005) and lower power consumption Shamah et al. (2001), but has the disadvantages of low maneuverability and need of an explicit mechanical steering subsystem Mandow et al.



Fig. 1. Examples of skid-steered vehicles: (Left) Skid-steered wheeled vehicle, (Right) Skid-steered tracked vehicle

(2007); Shamah et al. (2001); Siegwart & Nourbakhsh (2005). Differential steering is popular because it provides high maneuverability with a zero turning radius and has a simple steering configuration Siegwart & Nourbakhsh (2005); Zhang et al. (1998). However, it does not have strong traction and mobility over rough and loose terrain, and hence is seldom used for outdoor terrains. Like differential steering, skid steering leads to high maneuverability Caracciolo et al. (1999); Economou et al. (2002); Siegwart & Nourbakhsh (2005), faster response Martinez et al. (2005), and also has a simple Mandow et al. (2007); Petrov et al. (2000); Shamah et al. (2001) and robust mechanical structure Kozłowski & Pazderski (2004); Mandow et al. (2007); Yi, Zhang, Song & Jayasuriya (2007). In contrast, it also leads to strong traction and high mobility Petrov et al. (2000), which makes it suitable for all-terrain traversal.

Many of the difficulties associated with modeling and operating both classes of skid-steered vehicles arise from the complex wheel (or track) and terrain interaction Mandow et al. (2007); Yi, Song, Zhang & Goodwin (2007). For Ackerman-steered or differential-steered vehicles, the wheel motions may often be accurately modeled by pure rolling, while for skid-steered vehicles in general curvilinear motion, the wheels (or tracks) roll and slide at the same time Mandow et al. (2007); O. Chuy et al. (2009); Yi, Song, Zhang & Goodwin (2007); Yi, Zhang, Song & Jayasuriya (2007). This makes it difficult to develop kinematic and dynamic models that accurately describe the motion. Other disadvantages are that the motion tends to be energy inefficient, difficult to control Kozłowski & Pazderski (2004); Martinez et al. (2005), and for wheeled vehicles, the tires tend to wear out faster Golconda (2005).

A kinematic model of a skid-steered wheeled vehicle maps the wheel velocities to the vehicle velocities and is an important component in the development of a dynamic model. In contrast to the kinematic models for Ackerman-steered and differential-steered vehicles, the kinematic model of a skid-steered vehicle is dependent on more than the physical dimensions of the vehicle since it must take into account vehicle sliding and is hence terrain-dependent Mandow et al. (2007); Wong (2001). In Mandow et al. (2007); Martinez et al. (2005) a kinematic model of a skid-steered vehicle was developed by assuming a certain equivalence with a kinematic model of a differential-steered vehicle. This was accomplished by experimentally determining the instantaneous centers of rotation (ICRs) of the sliding velocities of the left

and right wheels. An alternative kinematic model that is based on the slip ratios of the wheels has been presented in Song et al. (2006); Wong (2001). This model takes into account the longitudinal slip ratios of the left and right wheels. The difficulty in using this model is the actual detection of slip, which cannot be computed analytically. Hence, developing practical methods to experimentally determine the slip ratios is an active research area Endo et al. (2007); Moosavian & Kalantari (2008); Nagatani et al. (2007); Song et al. (2008).

To date, there is very little published research on the experimentally verified dynamic models for general motion of skid-steered vehicles, especially wheeled vehicles. The main reason is that it is hard to model the tire (or track) and terrain interaction when slipping and skidding occur. (For each vehicle wheel, if the wheel linear velocity computed using the angular velocity of the wheel is larger than the actual linear velocity of the wheel, slipping occurs, while if the computed wheel velocity is smaller than the actual linear velocity, skidding occurs.) The research of Caracciolo et al. (1999) developed a dynamic model for planar motion by considering longitudinal rolling resistance, lateral friction, moment of resistance for the vehicle, and also the nonholonomic constraint for lateral skidding. In addition, a model-based nonlinear controller was designed for trajectory tracking. However, this model uses Coulomb friction to describe the lateral sliding friction and moment of resistance, which contradicts the experimental results Wong (2001); Wong & Chiang (2001). In addition, it does not consider any of the motor properties. Furthermore, the results of Caracciolo et al. (1999) are limited to simulation without experimental verification.

The research of Kozłowski & Pazderski (2004) developed a planar dynamic model of a skid-steered vehicle, which is essentially that of Caracciolo et al. (1999), using a different velocity vector (consisting of the longitudinal and angular velocities of the vehicle instead of the longitudinal and lateral velocities). In addition, the dynamics of the motors, though not the power limitations, were added to the model. Kinematic, dynamic and motor level control laws were explored for trajectory tracking. However, as in Caracciolo et al. (1999), Coulomb friction was used to describe the lateral friction and moment of resistance, and the results are limited to simulation. In Yi, Song, Zhang & Goodwin (2007) a functional relationship between the coefficient of friction and longitudinal slip is used to capture the interaction between the wheels and ground, and further to develop a dynamic model of skid-steered wheeled vehicle. Also, an adaptive controller is designed to enable the robot to follow a desired trajectory. The inputs of the dynamic model are the longitudinal slip ratios of the four wheels. However, the longitudinal slip ratios are difficult to measure in practice and depend on the terrain surface, instantaneous radius of curvature, and vehicle velocity. In addition, no experiment is conducted to verify the reliability of the torque prediction from the dynamic model and motor saturation and power limitations are not considered. In Wang et al. (2009) the dynamic model from Yi, Song, Zhang & Goodwin (2007) is used to explore the motion stability of the vehicle, which is controlled to move with constant linear velocity and angular velocity for each half of a lemniscate to estimate wheel slip. As in Yi, Song, Zhang & Goodwin (2007), no experiment is carried out to verify the fidelity of the dynamic model.

The most thorough dynamic analysis of a skid-steered vehicle is found in Wong (2001); Wong & Chiang (2001), which consider steady-state (i.e., constant linear and angular velocities) dynamic models for circular motion of *tracked* vehicles. A primary contribution of this research is that it proposes and then provides experimental evidence that in the track-terrain interaction the shear stress is a particular function of the shear displacement. This model differs from the Coulomb model of friction, adopted in Caracciolo et al. (1999); Kozłowski & Pazderski (2004), which essentially assumes that the maximum shear stress is obtained as

soon as there is any relative movement between the track and the ground. This research also provides detailed analysis of the longitudinal and lateral forces that act on a tracked vehicle. But their results had not been extended to skid-steered *wheeled* vehicles. In addition, they do not consider vehicle acceleration, terrain elevation, actuator limitations, or the vehicle control system.

In the existing literature there are very few publications that consider power modeling of skid-steered vehicles. The research of Kim & Kim (2007) provides an energy model of a skid-steered wheeled vehicle in linear motion. This model is essentially the time integration of a power model and is derived from the dynamic model of a motor, including the energy loss due to the armature resistance and viscous friction as well as the kinetic energy of the vehicle. This research also uses the energy model to find the velocity trajectory that minimizes the energy consumption. However, the energy model only considers the dynamics of the motor, but does not include the mechanical dynamics of the vehicle and hence ignores the substantial energy consumption due to sliding friction. Because longitudinal friction and moment of resistance lead to substantial power loss when a skid-steered vehicle is in general curvilinear motion, the results of Kim & Kim (2007) cannot be readily extended to motion that is not linear.

The most thorough exploration of power modeling of a skid-steered (tracked) vehicle is presented in Morales et al. (2009) and Morales et al. (2006). This research develops an experimental power model of a skid-steered tracked vehicle from terrain's perspective. The power model includes the power loss drawn by the terrain due to sliding frictions, and also the power losses due to the traction resistance and the motor drivers. Based on another conceptual model, this research considers the case in which the inner track has the same velocity sign as the outer track and *qualitatively* describes the negative sliding friction of the inner track, which leads the corresponding motor to work as a generator. Experiments to apply the power model for navigation are also described. However, this research has two limitations that the current research seeks to overcome. First, as in Caracciolo et al. (1999); Kozłowski & Pazderski (2004), discussed above in the context of dynamic modeling of skid-steered vehicles, Coulomb's law is adopted to describe the sliding friction component in the power modeling, which can lead to incorrect predictions for larger turning radii. Second, since the power model is derived from the perspective of the terrain drawing power from the tracks, it does not appear possible to quantify the power consumption of the left and right side motors. This is important since the motion of the vehicles can be dependent upon the power limitations of the motors.

Building upon the research in Wong (2001); Wong & Chiang (2001), this chapter will develop dynamic models of a skid-steered wheeled vehicle for general curvilinear planar (2D) motion. As in Wong (2001); Wong & Chiang (2001) the modeling is based upon the functional relationship of shear stress to shear displacement. Practically, this means that for a vehicle tire the shear stress varies with the turning radius. This chapter also includes models of the saturation and power limitations of the actuators as part of the overall vehicle model.

Using the developed dynamic model for 2D general curvilinear motion, this chapter will also develop power models of a skid-steered wheeled vehicle based on separate power models for left and right motors. The power model consists of two parts: (1) the mechanical power consumption, including the mechanical loss due to sliding friction and moment of resistance, and the power used to accelerate vehicle; and (2) the electrical power consumption, which is the electrical loss due to the motor electrical resistance. The mechanical power consumption is derived completely from the dynamic model, while the electrical power consumption is derived using the electric current predicted from this dynamic model along with circuit

theory. This chapter also discusses the interesting phenomenon that while the outer motor always consumes power, even though the velocity of inner wheel is always positive, as the turning radius decreases from infinity (corresponding to linear motion), the inner motor first consumes power, then generates power, and finally consumes power again.

In summary, we expect this chapter to make the following two fundamental contributions to dynamic modeling and power modeling of skid-steered wheeled vehicles:

1. **A paradigm for deriving dynamic models of skid-steered wheeled vehicles.** The modeling methodology will result in terrain-dependent models that describe general general planar (2D) motion.
2. **A paradigm for deriving power models of skid-steered wheeled vehicles based on dynamic models.** The power model of a skid-steered vehicle will be derived from vehicle dynamic models. The power model will be described from the perspective of the motors and includes both the mechanical power consumption and electrical power consumption. It can predict when a given trajectory is unachievable because the power limitation of one of the motors is violated.

2. Kinematics of a skid-steered wheeled vehicle

In this section, the kinematic model of a skid-steered wheeled vehicle is described and discussed. It is an important component in the development of the overall dynamic models and power models of a skid-steered wheeled vehicle.

To mathematically describe the kinematic models that have been developed for skid-steered vehicles, consider a wheeled vehicle moving at constant velocity about an instantaneous center of rotation as shown in Fig. 2.

The global and local coordinate frames are denoted respectively by X - Y and x - y . The variables v , $\dot{\phi}$ and R are respectively the translational velocity, angular velocity and turning radius of vehicle. The instantaneous centers of rotation for the left wheel and right wheel are given respectively by ICR_l and ICR_r . Note that ICR_l and ICR_r are the centers for left and right wheel treads (the parts of the tires that contact and slide on the terrain) Wong & Chiang (2001); Yi, Zhang, Song & Jayasuriya (2007), i.e., they are the centers for the sliding velocities of these contacting treads, but not the centers for the actual velocities of each wheel. It has been shown that the three ICRs are in the same line, which is parallel to the x -axis of the local frame Mandow et al. (2007); Yi, Zhang, Song & Jayasuriya (2007).

In the x - y frame, the coordinates of ICR , ICR_l and ICR_r are described as (x_{ICR}, y_{ICR}) , (x_{ICR_l}, y_{ICR_l}) and (x_{ICR_r}, y_{ICR_r}) . The vehicle velocity is denoted as $u = [v_x \ v_y \ \dot{\phi}]^T$, where v_x and v_y are the components of v along the x and y axes. The angular velocities of the left and right wheels are denoted respectively by ω_l and ω_r . (Note that for both the left and right side of the vehicle the velocities of the front and rear wheels are the same since they are driven by the same belt, and hence, there is only one velocity associated with each side.) The parameters b , B and r are respectively the wheel width, the vehicle width, and the wheel radius.

An experimental kinematic model of a skid-steered wheeled vehicle that is developed in Mandow et al. (2007) is given by

$$\begin{bmatrix} v_x \\ v_y \\ \dot{\phi} \end{bmatrix} = \frac{r}{x_{ICR_r} - x_{ICR_l}} \begin{bmatrix} -y_{ICR} & y_{ICR} \\ x_{ICR_r} & -x_{ICR_l} \\ -1 & 1 \end{bmatrix} \begin{bmatrix} \omega_l \\ \omega_r \end{bmatrix} \quad (1)$$

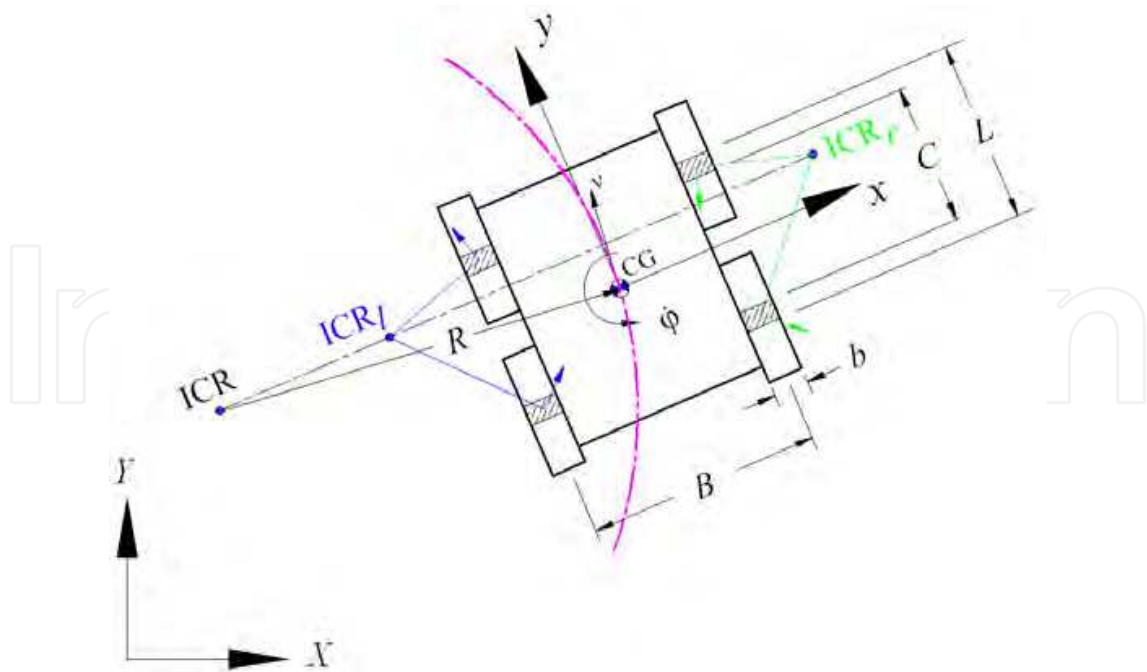


Fig. 2. The kinematics of a skid-steered wheeled vehicle and the corresponding instantaneous centers of rotation (ICRs)

If the skid-steered wheeled vehicle is symmetric about the x and y axes, then $y_{ICRl} = y_{ICRr} = 0$ and $x_{ICRl} = -x_{ICRr}$. Define the expansion factor α as the ratio of the longitudinal distance between the left and right wheels over the vehicle width, i.e.,

$$\alpha \triangleq \frac{x_{ICRr} - x_{ICRl}}{B}. \quad (2)$$

Then, for a symmetric vehicle the kinematic model (1) can be expressed as

$$\begin{bmatrix} v_y \\ \dot{\phi} \end{bmatrix} = \frac{r}{\alpha B} \begin{bmatrix} \frac{\alpha B}{2} & \frac{\alpha B}{2} \\ -1 & 1 \end{bmatrix} \begin{bmatrix} \omega_l \\ \omega_r \end{bmatrix}. \quad (3)$$

(Note that $v_x = 0$.)

The expansion factor α varies with the terrain. Experimental results show that the larger the rolling resistance, the larger the expansion factor. For a Pioneer 3-AT, $\alpha = 1.5$ for a vinyl lab surface and $\alpha > 2$ for a concrete surface. Equation (3) shows that the kinematic model of a skid-steered wheeled vehicle of width B is equivalent to the kinematic model of a differential-steered wheeled vehicle of width αB . Note that when $\alpha = 1$, (3) becomes the kinematic model for a differential-steered wheeled vehicle.

A more rigorously derived kinematic model for a skid-steered vehicle is presented in Moosavian & Kalantari (2008); Song et al. (2006); Wong (2001). This model takes into account the longitudinal slip ratios i_l and i_r of the left and right wheels and for symmetric vehicles is given by

$$\begin{bmatrix} v_y \\ \dot{\phi} \end{bmatrix} = \frac{r}{B} \begin{bmatrix} \frac{(1-i_l)B}{2} & \frac{(1-i_r)B}{2} \\ -(1-i_l) & (1-i_r) \end{bmatrix} \begin{bmatrix} \omega_l \\ \omega_r \end{bmatrix}, \quad (4)$$

where $i_l \triangleq (r\omega_l - v_{l_a})/(r\omega_l)$, $i_r \triangleq (r\omega_r - v_{r_a})/(r\omega_r)$ and v_{l_a} and v_{r_a} are the actual velocities of the left and right wheels. We have found that when

$$\frac{i_l}{i_r} = -\frac{\omega_r}{\omega_l} \text{ and } \alpha = \frac{1}{1 - \frac{2i_l i_r}{i_l + i_r}}, \quad (5)$$

(3) and (4) are identical. Currently, to our knowledge no analysis or experiments have been performed to verify the left hand equation in (5) and analyze its physical significance. However, for a limited range of turning radii experimentally derived expressions for i_l/i_r , essentially in terms of ω_l and ω_r , are given in Endo et al. (2007); Nagatani et al. (2007).

3. Dynamic modeling of a skid-steered wheeled vehicle

This section develops dynamic models of a skid-steered wheeled vehicle for the cases of general 2D motion. In contrast to dynamic models described in terms of the velocity vector of the vehicle Caracciolo et al. (1999); Kozłowski & Pazderski (2004), the dynamic models here are described in terms of the angular velocity vector of the wheels. This is because the wheel (specifically, the motor) velocities are actually commanded by the control system, so this model form is particularly beneficial for control and planning.

Following Kozłowski & Pazderski (2004), the dynamic model considering the nonholonomic constraint is given by

$$M\ddot{q} + C(q, \dot{q}) + G(q) = \tau, \quad (6)$$

where $q = [\theta_l \ \theta_r]^T$ is the angular displacement of the left and right wheels, $\dot{q} = [\omega_l \ \omega_r]^T$ is the angular velocity of the left and right wheels, $\tau = [\tau_l \ \tau_r]^T$ is the torque of the left and right motors, M is the mass matrix, $C(q, \dot{q})$ is the resistance term, and $G(q)$ is the gravitational term. The primary focus of the following subsection is the derivation of $C(q, \dot{q})$ to properly model the ground and wheel interaction. In the following content, it is assumed that the vehicle is symmetric and the center of gravity (CG) is at the geometric center.

When the vehicle is moving on a 2D surface, it follows from the model given in Kozłowski & Pazderski (2004), which is expressed in the local x - y coordinates, and the kinematic model (3) that M in (6) is given by

$$M = \begin{bmatrix} \frac{mr^2}{4} + \frac{r^2 I}{\alpha B^2} & \frac{mr^2}{4} - \frac{r^2 I}{\alpha B^2} \\ \frac{mr^2}{4} - \frac{r^2 I}{\alpha B^2} & \frac{mr^2}{4} + \frac{r^2 I}{\alpha B^2} \end{bmatrix}, \quad (7)$$

where m and I are respectively the mass and moment of inertia of the vehicle. Since we are considering planar motion, $G(q) = 0$. $C(q, \dot{q})$ represents the resistance resulting from the interaction of the wheels and terrain, including the rolling resistance, sliding frictions, and the moment of resistance, the latter two of which are modeled using Coulomb friction in Caracciolo et al. (1999); Kozłowski & Pazderski (2004). Assume that $\dot{q} = [\omega_l \ \omega_r]^T$ is a known constant, then $\ddot{q} = 0$ and (6) becomes

$$C(q, \dot{q}) = \tau. \quad (8)$$

Previous research Caracciolo et al. (1999); Kozłowski & Pazderski (2004) assumed that the shear stress takes on its maximum magnitude as soon as a small relative movement occurs between the contact surface of the wheel and terrain. Instead of using this theory for tracked vehicle, Wong (2001) and Wong & Chiang (2001) present experimental evidence to show that the shear stress of the tread is function of the shear displacement. The maximum shear stress is practically achieved only when the shear displacement exceeds a particular threshold. In this section, this theory will be applied to a skid-steered wheeled vehicle.

Based on the theory in Wong (2001); Wong & Chiang (2001), the shear stress τ_{ss} and shear displacement j relationship can be described as,

$$\tau_{ss} = p\mu(1 - e^{-j/K}), \quad (9)$$

where p is the normal pressure, μ is the coefficient of friction and K is the shear deformation modulus. K is a terrain-dependent parameter, like the rolling resistance and coefficient of friction Wong (2001).

Fig. 3 depicts a skid-steered wheeled vehicle moving counterclockwise (CCW) at constant linear velocity v and angular velocity $\dot{\phi}$ in a circle centered at O from position 1 to position 2. X - Y denotes the global frame and the body-fixed frames for the right and left wheels are given respectively by the x_r - y_r and x_l - y_l . The four contact patches of the wheels with the ground are shadowed in Fig. 3 and L and C are the patch-related distances shown in Fig. 3. It is assumed that the vehicle is symmetric and the center of gravity (CG) is at the geometric center. Note that because ω_l and ω_r are known, v_y and $\dot{\phi}$ can be computed using the vehicle kinematic model (3), which enables the determination of the radius of curvature R since $v_y = R\dot{\phi}$.

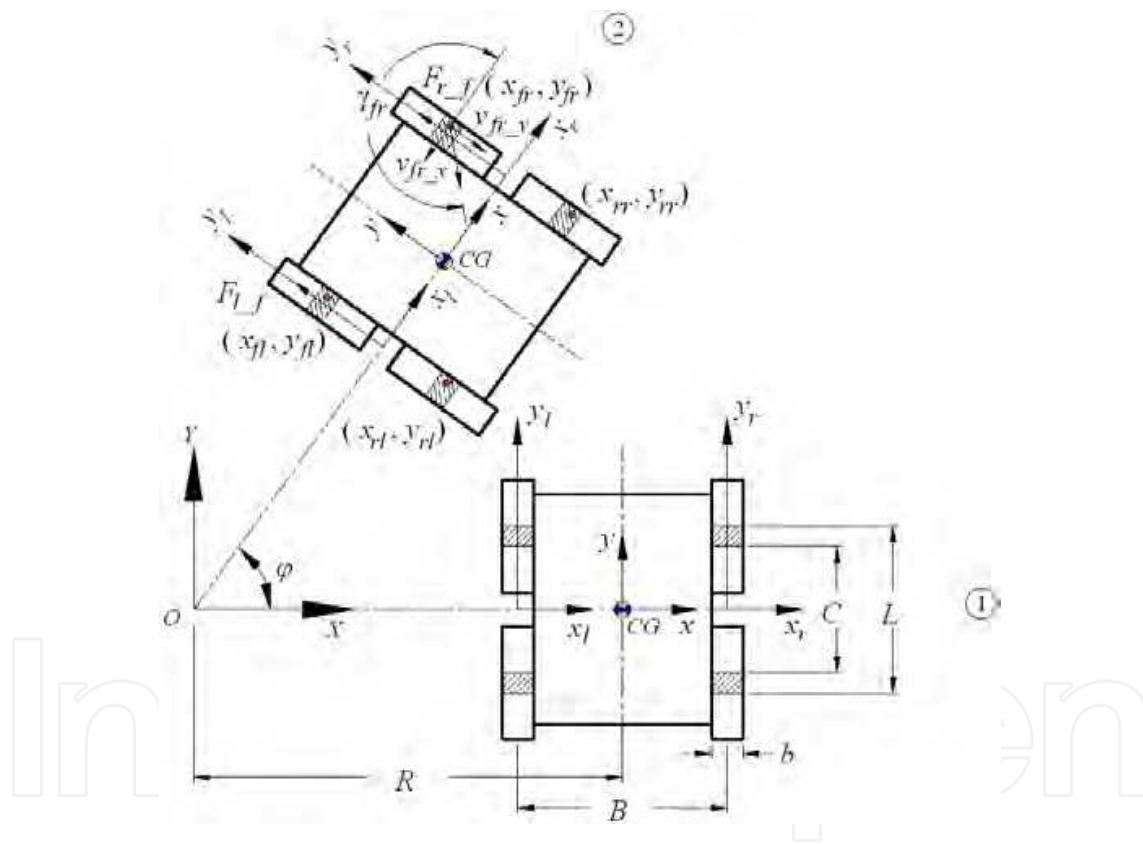


Fig. 3. Circular motion of a skid-steered wheeled vehicle

In the x_r - y_r frame consider an arbitrary point on the contact patch of the front right wheel with coordinates (x_{fr}, y_{fr}) . This contact patch is *not* fixed on the tire, but is the part of the tire that contacts the ground. The time interval t for this point to travel from an initial contact point $(x_{fr}, L/2)$ to (x_{fr}, y_{fr}) is,

$$t = \int_{y_{fr}}^{L/2} \frac{1}{r\omega_r} dy_r = \frac{L/2 - y_{fr}}{r\omega_r}. \quad (10)$$

During the same time, the vehicle has moved from position 1 to position 2 with an angular displacement of φ . The sliding velocities of point (x_{fr}, y_{fr}) in the x_r and y_r directions are denoted by v_{fr_x} and v_{fr_y} . Therefore,

$$v_{fr_x} = -y_{fr}\dot{\varphi}, \quad v_{fr_y} = (R + B/2 + x_{fr})\dot{\varphi} - r\omega_r. \quad (11)$$

The resultant sliding velocity v_{fr} and its angle γ_{fr} in the x_r - y_r frame are

$$v_{fr} = \sqrt{v_{fr_x}^2 + v_{fr_y}^2}, \quad \gamma_{fr} = \pi + \arctan\left(\frac{v_{fr_y}}{v_{fr_x}}\right). \quad (12)$$

Note that when the wheel is sliding, the direction of friction is opposite to the sliding velocity, and if the vehicle is in pure rolling, v_{fr_x} and v_{fr_y} are zero.

In order to calculate the shear displacement of this reference point, the sliding velocities need to be expressed in the global X-Y frame. Let v_{fr_X} and v_{fr_Y} denote the sliding velocities in the X and Y directions. Then, the transformation between the local and global sliding velocities is given by,

$$\begin{bmatrix} v_{fr_X} \\ v_{fr_Y} \end{bmatrix} = \begin{bmatrix} \cos \varphi & -\sin \varphi \\ \sin \varphi & \cos \varphi \end{bmatrix} \begin{bmatrix} v_{fr_x} \\ v_{fr_y} \end{bmatrix}. \quad (13)$$

The shear displacements j_{fr_X} and j_{fr_Y} in the X and Y directions can be expressed as

$$\begin{aligned} j_{fr_X} &= \int_0^t v_{fr_X} dt = \int_{y_{fr}}^{L/2} (v_{fr_x} \cos \varphi - v_{fr_y} \sin \varphi) \frac{1}{r\omega_r} dy_r \\ &= (R + B/2 + x_{fr}) \cdot \left\{ \cos \left[\frac{(L/2 - y_{fr})\dot{\varphi}}{r\omega_r} \right] - 1 \right\} - y_{fr} \sin \left[\frac{(L/2 - y_{fr})\dot{\varphi}}{r\omega_r} \right], \end{aligned} \quad (14)$$

$$\begin{aligned} j_{fr_Y} &= \int_0^t v_{fr_Y} dt = \int_{y_{fr}}^{L/2} (v_{fr_x} \sin \varphi + v_{fr_y} \cos \varphi) \frac{1}{r\omega_r} dy_r \\ &= (R + B/2 + x_{fr}) \cdot \sin \left[\frac{(L/2 - y_{fr})\dot{\varphi}}{r\omega_r} \right] - L/2 + y_{fr} \cos \left[\frac{(L/2 - y_{fr})\dot{\varphi}}{r\omega_r} \right]. \end{aligned} \quad (15)$$

The resultant shear displacement j_{fr} in the X-Y frame is given by, $j_{fr} = \sqrt{j_{fr_X}^2 + j_{fr_Y}^2}$. Similarly, it can be shown that for the reference point (x_{rr}, y_{rr}) in the rear right wheel the angle of the sliding velocity γ_{rr} in the x_r - y_r frame is

$$\gamma_{rr} = \arctan \left[\frac{(R + B/2 + x_{rr})\dot{\varphi} - r\omega_r}{-y_{rr}\dot{\varphi}} \right], \quad (16)$$

and the shear displacements j_{rr_X} and j_{rr_Y} are given by

$$j_{rr_X} = (R + B/2 + x_{rr}) \cdot \left\{ \cos \left[\frac{(-C/2 - y_{rr})\dot{\varphi}}{r\omega_r} \right] - 1 \right\} - y_{rr} \sin \left[\frac{(-C/2 - y_{rr})\dot{\varphi}}{r\omega_r} \right], \quad (17)$$

$$j_{rr_Y} = (R + B/2 + x_{rr}) \cdot \sin \left[\frac{(-C/2 - y_{rr})\dot{\varphi}}{r\omega_r} \right] + C/2 + y_{rr} \cos \left[\frac{(-C/2 - y_{rr})\dot{\varphi}}{r\omega_r} \right]. \quad (18)$$

and the magnitude of the resultant shear displacement j_{rr} is $j_{rr} = \sqrt{j_{rr_X}^2 + j_{rr_Y}^2}$.

The friction force points in the opposite direction of the sliding velocity. Using j_{fr} and j_{rr} , derived above, with (9) and integrating along the contact patches yields that the longitudinal sliding friction of the right wheels F_{r_f} can be expressed as

$$F_{r_f} = \int_{C/2}^{L/2} \int_{-b/2}^{b/2} p_r \mu_r (1 - e^{-j_{fr}/K_r}) \sin(\pi + \gamma_{fr}) dx_r dy_r + \int_{-L/2}^{-C/2} \int_{-b/2}^{b/2} p_r \mu_r (1 - e^{-j_{rr}/K_r}) \sin(\pi + \gamma_{rr}) dx_r dy_r, \quad (19)$$

where p_r , μ_r and K_r are respectively the normal pressure, coefficient of friction, and shear deformation modulus of the right wheels. While most of the parameters in (19) can be directly measured, as discussed further below, the parameters μ_r and K_r must be estimated.

Let f_{r_r} denote the rolling resistance of the right wheels, including the internal locomotion resistance such as resistance from belts, motor windings and gearboxes Morales et al. (2006). The complete resistance torque τ_{r_Res} from the ground to the right wheel is given by

$$\tau_{r_Res} = r(F_{r_f} + f_{r_r}). \quad (20)$$

Since ω_r is constant, the input torque τ_r from right motor will compensate for the resistance torque, such that

$$\tau_r = \tau_{r_Res}. \quad (21)$$

The above discussion is for the right wheels. Exploiting the same derivation process, one can obtain analytical expressions for the shear displacements j_{fl} and j_{rl} of the front and rear left wheels, and the angles of the sliding velocity γ_{fl} and γ_{rl} . The longitudinal sliding friction of the left wheels F_{l_f} is then given by

$$F_{l_f} = \int_{C/2}^{L/2} \int_{-b/2}^{b/2} p_l \mu_l (1 - e^{-j_{fl}/K_l}) \sin(\pi + \gamma_{fl}) dx_l dy_l + \int_{-L/2}^{-C/2} \int_{-b/2}^{b/2} p_l \mu_l (1 - e^{-j_{rl}/K_l}) \sin(\pi + \gamma_{rl}) dx_l dy_l, \quad (22)$$

where p_l , μ_l and K_l are respectively the normal pressure, coefficient of friction, and shear deformation modulus of the left wheels. Denote the rolling resistance of the left wheels as f_{l_r} . The input torque τ_l of the left motor equals the resistance torque of the left wheel τ_{l_Res} , such that

$$\tau_l = \tau_{l_Res} = r(F_{l_f} + f_{l_r}). \quad (23)$$

Fig. 4 compares the resistance torque prediction of τ_{l_Res} and τ_{r_Res} using shear stress and shear displacement function (9) and Coulomb's law when the skid-steered wheeled vehicle of Fig. 13 is in steady state rotation.

$$\tau_{ss} = p\mu \text{ (Coulomb's Law)} \quad (24)$$

It is seen that Coulomb's law leads to a resistance torque that has the same constant value for all turning radii, which contradicts the experimental results shown in Wong (2001); Wong & Chiang (2001) for tracked vehicles and below in Fig. 15 for wheeled vehicles.

Using (21) and the left equation of (23) with (8) yields

$$C(q, \dot{q}) = [\tau_{l_Res} \ \tau_{r_Res}]^T. \quad (25)$$

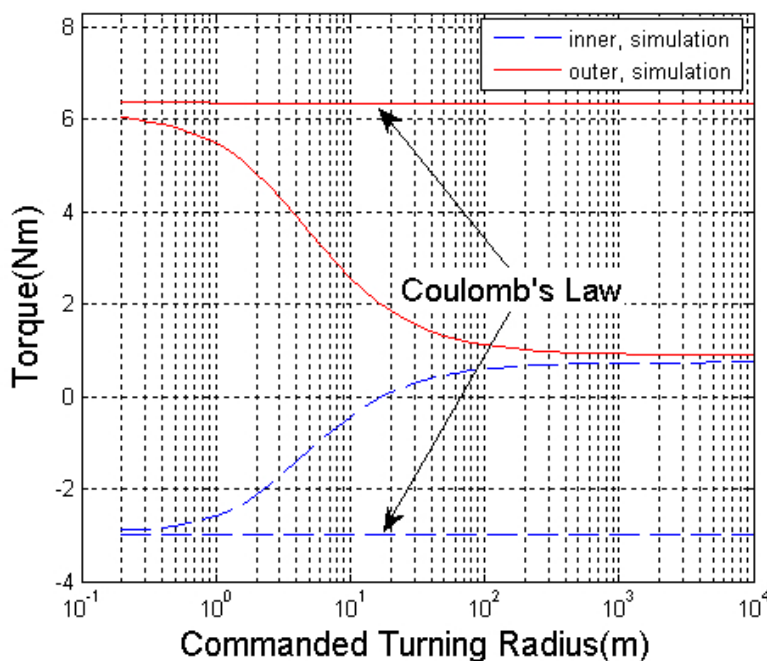


Fig. 4. Inner and outer motor resistance torque prediction using function (9) and Coulomb’s law when vehicle is in steady state rotation.

Substituting (7), (25) and $G(q) = 0$ into (6) yields a dynamic model that can be used to predict 2D movement for the skid-steered vehicle:

$$\begin{bmatrix} \frac{mr^2}{4} + \frac{r^2I}{\alpha B^2} & \frac{mr^2}{4} - \frac{r^2I}{\alpha B^2} \\ \frac{mr^2}{4} - \frac{r^2I}{\alpha B^2} & \frac{mr^2}{4} + \frac{r^2I}{\alpha B^2} \end{bmatrix} \ddot{q} + \begin{bmatrix} \tau_{l_Res} \\ \tau_{r_Res} \end{bmatrix} = \begin{bmatrix} \tau_l \\ \tau_r \end{bmatrix}. \tag{26}$$

In summary, in order to obtain (25), the shear displacement calculation of (14), (15), (17) and (18) is the first step. The inputs to these equations are the left and right wheel angular velocities ω_l and ω_r . The shear displacements are employed in (19) and (22) to obtain the right and left sliding friction forces, F_{r_f} and F_{l_f} . Next, the sliding friction forces and rolling resistances are substituted into (20) and (23) to calculate the right and left resistance torques, which determine $C(q, \dot{q})$ using (25).

4. Power modeling of a skid-steered wheeled vehicle

This section derives power models for a skid-steered wheeled vehicle, moving as in Fig. 3. The foundation for modeling the power consumption model is the dynamic model of Section 3. The power consumption for each side of the vehicle includes the mechanical power consumption due to the motion of the wheels and the electrical power consumption due to the electrical resistance of the motors. The total power consumption of the vehicle is the sum of the power consumption of the left and right sides.

Assume that a skid-steered wheeled vehicle moves CCW about an instantaneous center of rotation (see Fig. 3). The circuit diagram for each side of the vehicle is shown in Fig. 5. Each circuit includes a battery, motor controller, motor M and the motor electrical resistance R_e . In Fig. 5 ω_l and ω_r are the angular velocities of the left and right wheels, U_l and U_r are the output voltages of the left and right motor controllers, and i_l and i_r are the currents of the left

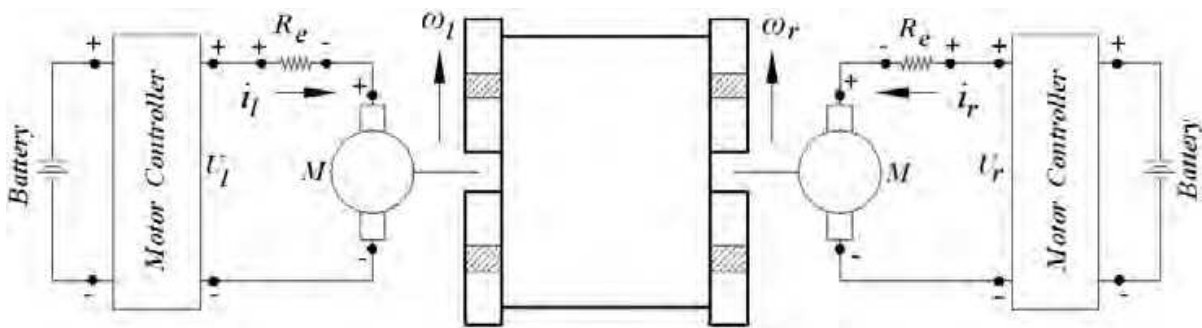


Fig. 5. The circuit layout for the left and right side of a skid-steered wheeled vehicle.

and right circuits. For the experimental vehicle used in this research (the modified Pioneer 3-AT shown in Fig. 13), ω_l and ω_r are always positive¹.

The electric model of a DC motor at steady state is given by Rizzoni (2000),

$$V_a = E_b + R_a I_a, \quad (27)$$

where V_a is the supply voltage to the motor, R_a is the motor armature resistance, I_a is the motor current, and E_b is the back EMF. The power consumption P_a of a DC motor is given by $P_a = V_a I_a$. Hence, multiplying (27) by I_a yields

$$P_a = V_a I_a = P_e + R_a I_a^2, \quad (28)$$

where P_e is the portion of the electric power converted to mechanical power by the motor and is given by

$$P_e = E_b I_a. \quad (29)$$

The mechanical power P_m of a DC motor is given by

$$P_m = \omega_m \tau, \quad (30)$$

where ω_m and τ are respectively the angular velocity and applied torque of the motor. For ideal energy-conversion case Rizzoni (2000),

$$P_m = P_e. \quad (31)$$

Substituting (29), (30) and (31) into (28) yields the power model of a DC motor used in the analysis of this research,

$$P_a = \omega_m \tau + R_a I_a^2. \quad (32)$$

In (32), the first term is the mechanical power consumption, which includes the power to compensate the left and right sliding frictions and the moment of resistance along with the power to accelerate the motor, and the second term is the electrical power consumption due to the motor electric resistance, which is dissipated as heat.

Using (32), the power consumed by the right motor P_r can be expressed as,

$$P_r = U_r i_r = P_{r,m} + P_{r,e}, \quad (33)$$

¹ Due to the torque limitations of the motors in the experimental vehicle, the minimum achievable turning radius is larger than half the width of the vehicle. This implies that the instantaneous radius of curvature is located outside of the vehicle body so that ω_l and ω_r are always positive.

where $P_{r,m}$ and $P_{r,e}$ are the mechanical power consumption and the electrical power consumption for the right side motor. In non ideal case, $P_{r,m}$ and $P_{r,e}$ in (33) are,

$$P_{r,m} = \frac{\tau_r \omega_r}{\eta}, \quad (34)$$

$$P_{r,e} = i_r^2 R_e, \quad (35)$$

where τ_r and ω_r are the same as in (26) in Section 3, and η is the motor efficiency. For the right side motor, the output torque τ_r determined from the dynamic model (26) is given by

$$\tau_r = K_T i_r g_r \eta, \quad (36)$$

where K_T is the torque constant and g_r is the gear ratio. So the required current in right side of motor is,

$$i_r = \frac{\tau_r}{K_T g_r \eta}. \quad (37)$$

Plugging (37) into (35) yields,

$$P_{r,e} = \left(\frac{\tau_r}{K_T g_r \eta}\right)^2 R_e. \quad (38)$$

Substituting (34) and (38) into (33), the power model for the right (outer) motor is,

$$P_r = \frac{\tau_r \omega_r}{\eta} + \left(\frac{\tau_r}{K_T g_r \eta}\right)^2 R_e. \quad (39)$$

Notice that the only variables in (39) is the applied torques τ_r along with the angular velocities ω_r , which are available from the dynamic model in Chapter 3.

Similarly, for the left (inner) part of vehicle,

$$P_l = U_l i_l = P_{l,m} + P_{l,e}, \quad (40)$$

$$P_{l,m} = \frac{\tau_l \omega_l}{\eta}, \quad (41)$$

$$P_{l,e} = i_l^2 R_e, \quad (42)$$

$$\tau_l = K_T i_l, \quad (43)$$

$$P_{l,e} = \left(\frac{\tau_l}{K_T g_r \eta}\right)^2 R_e, \quad (44)$$

$$P_l = \frac{\tau_l \omega_l}{\eta} + \left(\frac{\tau_l}{K_T g_r \eta}\right)^2 R_e. \quad (45)$$

Let P denote the power that must be supplied by the motor drivers to the motors to enable the motion of a of a skid-steered wheeled vehicle and define the operator $\sigma : \mathbb{R} \rightarrow \mathbb{R}$ such that

$$\sigma(Q) = \begin{cases} Q & : Q \geq 0 \\ 0 & : Q < 0. \end{cases} \quad (46)$$

Then the entire power model of a skid-steered wheeled vehicle is,

$$P = \sigma(P_r) + \sigma(P_l). \quad (47)$$

Typically, one might expect to write $P = P_r + P_l$. However, since it turns out that P_l can be negative and that this generated power does not charge the battery in our research vehicle,

the more general form (47) is used. To enable the battery to be charged requires modifications of the motor controller, which was beyond the scope of this project.

In summary, given the input of the left wheel and right wheel angular velocities ω_l and ω_r , the first step in computing (45) and (39), the power models of the left motors and right motors, is the calculation of the left wheel and right wheel sliding frictions F_{l_f} and F_{r_f} using (22) and (19). The sliding frictions along with experimentally determined values of the rolling resistances f_{l_r} and f_{r_r} are then substituted into (23) and (20) to obtain the resistance torques $\tau_{l_{Res}}$ and $\tau_{r_{Res}}$, which are in turn substituted into the vehicle dynamic model (26) to obtain the left wheel and right wheel torques τ_l and τ_r . Next, the left and right wheel torques are substituted into (45) and (39) to calculate the power consumption of the left and right wheels. The entire power consumption of the vehicle may then be computed by substituting (45) and (39) into (47). While (45) and (39) are general equations for all DC motor driven vehicles, the τ_l and τ_r in (45) and (39) have to be calculated specifically from the skid-steered dynamic model (26).

4.1 Power models analysis

To better analyze the vehicle power model, consider the results from a series of simulations for CCW steady state rotation of the modified Pioneer 3-AT, the research platform shown in Fig. 13. For each simulation, the vehicle was commanded to have a linear velocity of 0.2 m/s. The commanded turning radius r_c is defined as the turning radius resulting from applying the wheel speeds, ω_l and ω_r , to a differential-steered kinematic model assuming no slip. The simulations corresponded to varying the commanded turning radius from $10^{-0.7}$ m to 10^4 m with the exponent increasing in increments of 0.1.

Fig. 6 and Fig. 7 were developed by using a simulation of the dynamic model (26) and respectively represent the applied torques and angular velocities for the left and right wheels. For both the right and left motors Fig. 8 compares the power consumption prediction obtained using the exponential friction model (9) with that obtained using Coulomb's law (24). (Both predictions were based on using the dynamic model (26) in conjunction with the power models (39) and (45).) It is seen that when Coulomb friction is assumed, as the turning radius increases, the power consumption of the outer motor does not converge to a small value ($\sim 3W$) as is predicted using exponential friction. Instead it converges to a much larger value ($\sim 35W$), which contradicts the experimental result in Fig. 16, which is almost identical to the exponential friction prediction. Fig. 9 further shows that the two models can yield dramatic differences in their predictions of the power consumption of the entire vehicle.

For the right motor Fig. 10 shows the total power consumption resulting from (39) along with its mechanical power component from (34) and its electrical power component from (35). Fig. 11 displays the same power information for the left motor using (45), (41), and (42). Although these curves correspond to a specific commanded linear velocity (0.2m/s), the shapes of these curves are typical of all velocities that have been simulated. Note that in these figures and the following discussion, $\underline{r} \approx 10^0$ m and $\bar{r} \approx 10^{1.1}$ m.

From (26), it is seen that when a vehicle is in steady state rotation,

$$\tau_{l_{Res}} = \tau_l, \quad \tau_{r_{Res}} = \tau_r, \quad (48)$$

which implies that for vehicle steady state rotation τ_l and τ_r only need to compensate for the resistance torques. So τ_l , τ_r in Fig. 6 also represent the resistance torques $\tau_{l_{Res}}$, $\tau_{r_{Res}}$ for vehicle steady state rotation.

Below, Fig. 6, Fig. 7 and Fig. 8 are used to analyze the current, voltage, and power consumption of each motor in greater detail. Particular attention is given to the inner (left) motor since it sometimes generates power.

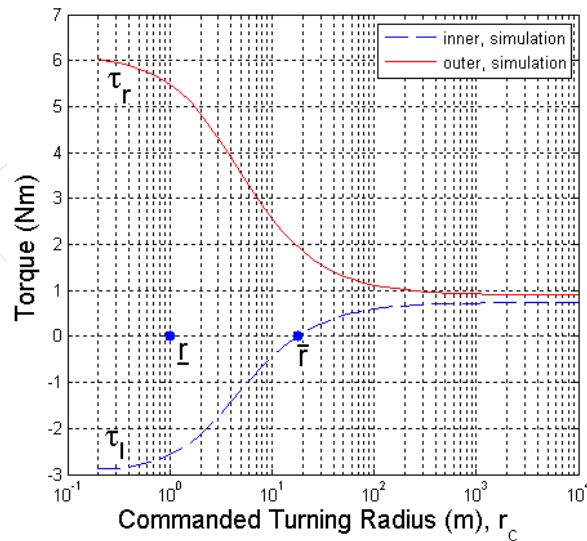


Fig. 6. Steady-state, inner and outer wheel torques vs. commanded turning radius, obtained via simulation of the dynamic model, for a commanded linear velocity of 0.2 m/s on the lab vinyl surface.

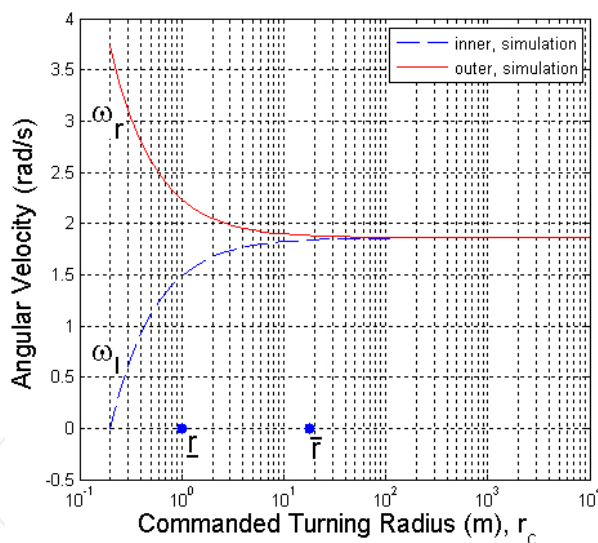


Fig. 7. Steady-state, inner and outer wheel angular velocities vs. commanded turning radius, obtained via simulation of the dynamic model for the conditions of Fig. 6.

Analysis of the Vehicle’s Outer (Right) Side

Fig. 6, Fig. 7 and Fig. 8 show that τ_r , ω_r and P_r are always positive. From (36) and (33), it follows that i_r and U_r are also positive. Therefore, for the right side of the vehicle,

$$i_r > 0, U_r > 0, P_r > 0, \tag{49}$$

which implies that the outer motor always consumes power. The direction of current flow, and the voltage of the motor controller, motor resistance and motor have the same signs as in Fig. 5.

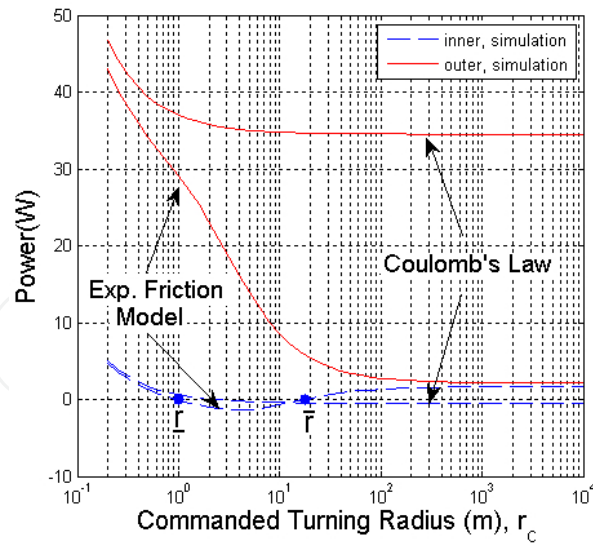


Fig. 8. Power prediction for the inner and the outer motors vs. commanded turning radius using exponential friction model (9) and Coulomb's law.

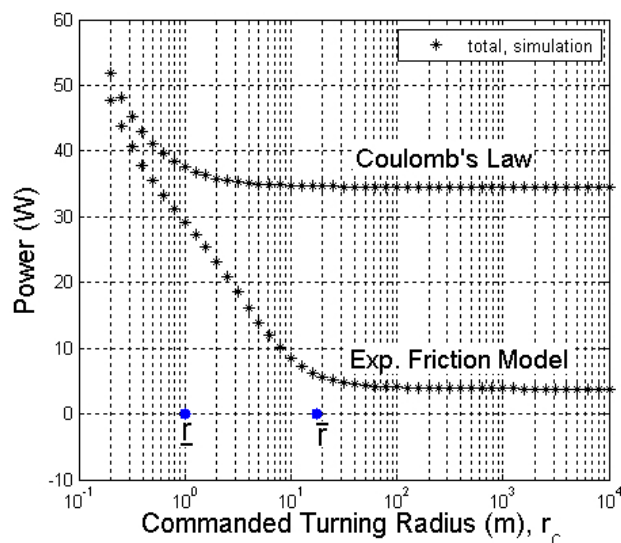


Fig. 9. Power prediction for the whole vehicle corresponding to Fig. 8 using exponential friction model (9) and Coulomb's law.

For the outer side of vehicle Fig. 10 shows that the mechanical power consumption and electrical power consumption are nearly equal for each turning radius². (As discussed after (32), only the mechanical power is converted into motion while the electrical power consumption is dissipated (or wasted) as heat.) In this case, the power source is always the battery operating through the motor controller,³ while the motor shaft motion consumes mechanical power and the motor electrical resistance consumes electrical power. Referring to (47),

$$\sigma(P_r) = P_r, \quad (50)$$

² As the motor electrical resistance decreases, the electrical power consumption will be smaller than the mechanical power consumption.

³ Some of the battery's power is dissipated as heat in the motor controller's resistance. See Fig. 5

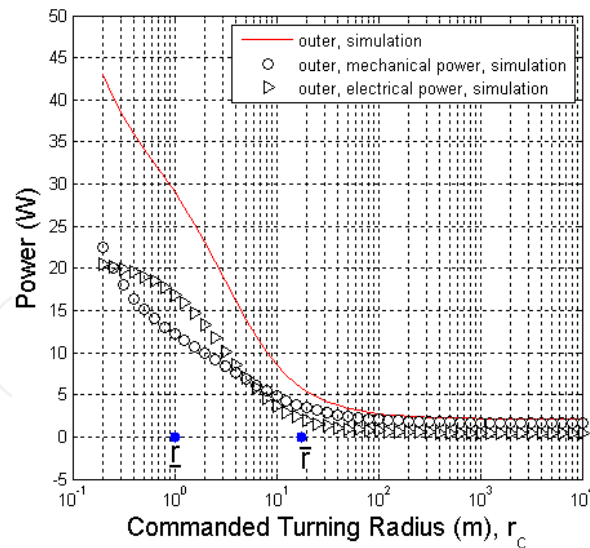


Fig. 10. Outer motor power comparison: outer total power consumption, outer mechanical power consumption and outer electrical power consumption, obtained via simulation of the dynamic model for the conditions of Fig. 6.

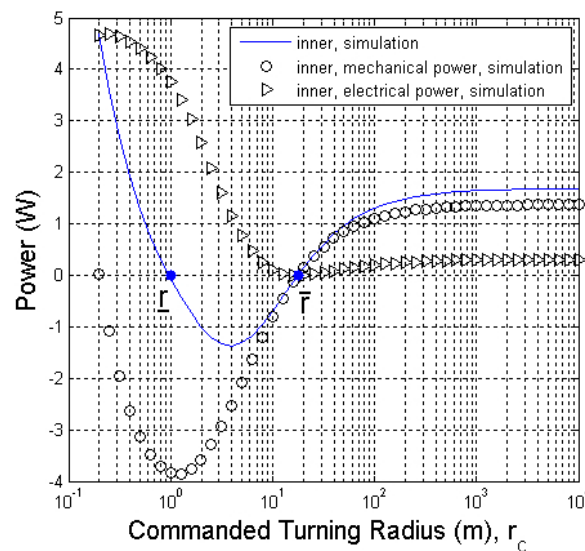


Fig. 11. Inner motor power comparison: inner total power consumption, inner mechanical power consumption and inner electrical power consumption, obtained via simulation of the dynamic model for the conditions of Fig. 6.

where P_r is given by (39).

Analysis of the Vehicle’s Inner (Left) Side

Fig. 6 shows that τ_l can be either positive or negative, Fig. 7 shows that ω_l is positive, while Fig. 8 shows that P_l can be either positive or negative. The signs of τ_l and P_l depend on whether the commanded turning radius r_c is in one of three regions: 1) $r_c \geq \bar{r}$, 2) $r_l < r_c < \bar{r}$, and 3) $r_c \leq r_l$. These three cases are now analyzed.

Case 1 ($r_c \geq \bar{r}$, $P_l > 0$): Fig. 6, Fig. 7 and Fig. 8 show that $\tau_l > 0$, $\omega_l > 0$ and $P_l > 0$. From (43) and (40), it follows $i_l > 0$, $U_l > 0$. Therefore, for the left side of the vehicle in this case,

$$i_l > 0, U_l > 0, P_l > 0, \tag{51}$$

which implies the left motor consumes power. The direction of the motor current flow and voltage are as shown in Fig. 5.

Fig. 11 shows that for each commanded turning radius r_c satisfying $r_c \geq \bar{r}$ the total motor power consumption is dominated by the mechanical power consumption although there is a small amount of electrical power consumption. In this case, the power source is the motor controller system, while the motor shaft motion consumes mechanical power and the motor electrical resistance consumes electrical power. Referring to (47),

$$\sigma(P_l) = P_l, \quad (52)$$

where P_l is given by (45).

Case 2 ($\underline{r} < r_c < \bar{r}$, $P_l < 0$): Fig. 6, Fig. 7 and Fig. 8 show that $\tau_l < 0$, $\omega_l > 0$ and $P_l < 0$. From (43) and (40), it follows $i_l < 0$, $U_l > 0$. Therefore, for the left side of the vehicle in this case,

$$i_l < 0, U_l > 0, P_l < 0, \quad (53)$$

which implies that the left motor generates power. In Fig. 5 the direction of i_l and the voltage drop across R_e are reversed, while the motor controller voltage U_l and that of the motor remain as shown.

Fig. 11 shows that for each commanded turning radius r_c satisfying $\underline{r} < r_c < \bar{r}$ the mechanical power consumption is negative, and hence the motor shaft motion does not consume power but on the contrary generates power from the terrain. This is because when the vehicle rotates, the outer wheel drags the inner wheel through the vehicle body Morales et al. (2009), which leads to the backward sliding friction for the inner wheel and the generation of power for the inner motor from terrain. Since the mechanically generated power is larger than the electrical power consumption, there is a net power generation that is consumed by the motor controller system. In this case, the power source is the motor shaft, while the motor electrical resistance and the motor controller system consume power. Referring to (47),

$$\sigma(P_l) = 0. \quad (54)$$

Case 3 ($r_c \leq \underline{r}$, $P_l > 0$): Fig. 6, Fig. 7 and Fig. 8 show that $\tau_l < 0$, $\omega_l > 0$ and $P_l > 0$. From (43) and (40), it follows $i_l < 0$, $U_l < 0$. Therefore, for the left side of the vehicle in this case,

$$i_l < 0, U_l < 0, P_l > 0, \quad (55)$$

which implies that the left motor consumes power. In Fig. 5 the direction of i_l , the voltage drop across the R_e and the motor controller voltage U_l are reversed, while the voltage sign of the motor remains the same.

Fig. 11 shows for each commanded turning radius r_c satisfying $r_c \leq \underline{r}$ the mechanical power consumption is negative, which means, as in Case 2, the motor shaft motion does not consume power but generates power from terrain. However, unlike Case 2, the generated mechanical power is smaller than the electrical power consumption. Hence, there is a net power consumption and the motor controller system still has to supply power. In this case, the power sources are the motor shaft and the motor controller system, while the motor electrical resistance consumes power. Referring to (47),

$$\sigma(P_l) = P_l, \quad (56)$$

where P_l is given by (45).

Analysis of the Power Consumption of the Entire Vehicle

The overall power consumption of the vehicle is due to the power consumption of both the inner and outer motors and is shown in Fig. 8. Fig. 12 shows the percentage of the overall power consumption of the vehicle due to mechanical power consumption and electrical power consumption. It is of interest to note that when $r_c \geq \bar{r}$, the mechanical power consumption is dominant, while as r_c decreases in value from \bar{r} the electrical heat dissipation eventually dominates. This indicates that in motion planning, as might be expected, it is more energy efficient to plan for trajectories with large turning radii.

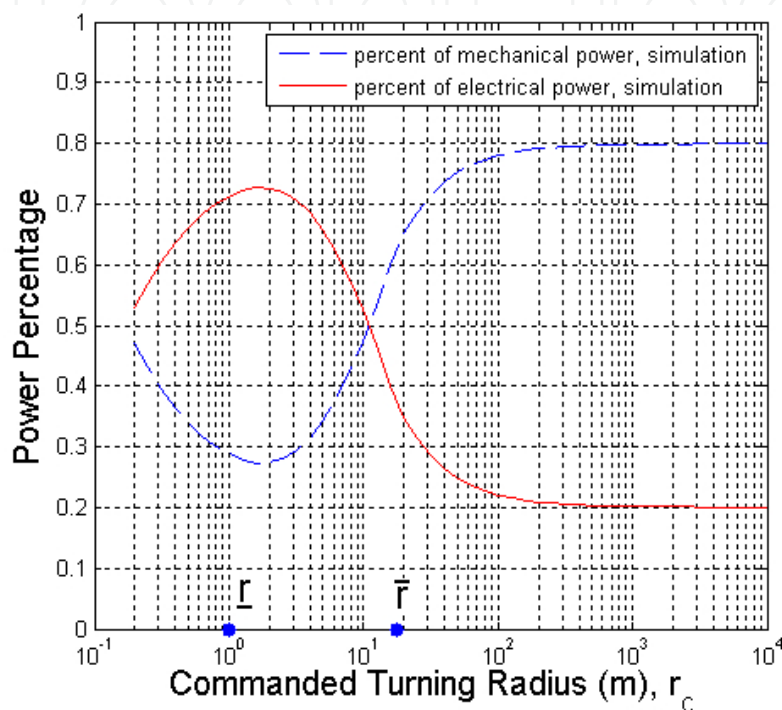


Fig. 12. Mechanical power and electrical power consumption percentages vs. commanded turning radius, obtained via simulation of the dynamic model, for the conditions of Fig. 6.

In summary, analysis of the power models of the right and left motors reveal the interesting phenomenon that for vehicle steady state rotation while the outer motor always consumes power, as the vehicle turning radius decreases, the inner motor first consumes, then generates and finally consumes power again. Since Fig. 8 is generated using the the power model (45), the model enables prediction of the two transition turning radii \underline{r} and \bar{r} .

5. Experimental results

This section presents the experiment and simulation results to verify the proposed dynamic models and power models in this chapter.

The experimental platform is the modified Pioneer 3-AT shown in Fig. 13. The original, nontransparent, speed controller from the company was replaced by a PID controller and motor controller. PC104 boards replaced the original control system boards that came with the vehicle. Two current sensors were mounted on each side of the vehicle to provide real time measurement of the motors' currents. It was modified to run on the QNX realtime operating system with a control sampling rate of 1KHz. The mobile robot can be commanded with a linear velocity and turning radius.



Fig. 13. Modified Pioneer 3-AT

5.1 Steady state rotation for different turning radii

In this subsection, 2D steady state rotation results for different turning radii are presented. For a vehicle commanded linear velocity of 0.2m/s and turning radius changing from $10^{-0.7}$ m to 10^4 m, Fig. 14 shows the experimental and simulation wheel angular velocity vs. commanded radius, Fig. 15 shows the experimental and simulation applied torques vs. commanded radius and Fig. 16 shows the experimental and simulated power consumption vs. commanded radius. In all figures there is good correspondence between the experimental and simulated results. If shear stress is not a function of shear displacement, but instead takes on a maximum value when there is a small relative movement between wheel and terrain, the left and right motor torques should be constant for different commanded turning radii, a phenomenon not seen in Fig. 15. Instead this figure shows the magnitudes of both the left and right torques reduce as the commanded turning radius increases. The same trend is found in Wong (2001); Wong & Chiang (2001). Note that the three cases of inner motor power consumption are observed in the experimental results of Fig. 16.

5.2 Circular movement with motor power saturation

In terms of motion planning one advantage of using the separate motor power models (39) and (45) instead of relying completely on the entire vehicle power model (47) is that the separate models enable more accurate predictions of vehicle velocity when an individual motor experiences power saturation. For a given trajectory it is possible for the entire vehicle power consumption required to achieve that trajectory to be below the total power that can be provided by the motor drive systems, but the power consumption required for one of the motors to be above the power limitations of that motor's drive system. In this case the desired trajectory cannot be achieved.

For the modified Pioneer 3-AT of Fig. 13, the maximum linear velocity is 0.93 m/s. The power limitation for each side of the motor drive system is 51 w, and total power limitation is 102 w. Fig. 17 was generated using (39) and (45) and shows the power requirements for the inner and outer motors vs. commanded turning radius when the vehicle has a linear velocity of 0.7 m/s. It also shows a line corresponding to the 51 w power limitation of each of the motor drive systems.

For a vehicle commanded linear velocity of 0.7 m/s and turning radius of 1.2 m, the predicted inner and outer motor power requirements for a commanded turning radius of 1.2 m are marked using square symbols in Fig. 17. It is seen that the outer motor power consumption is

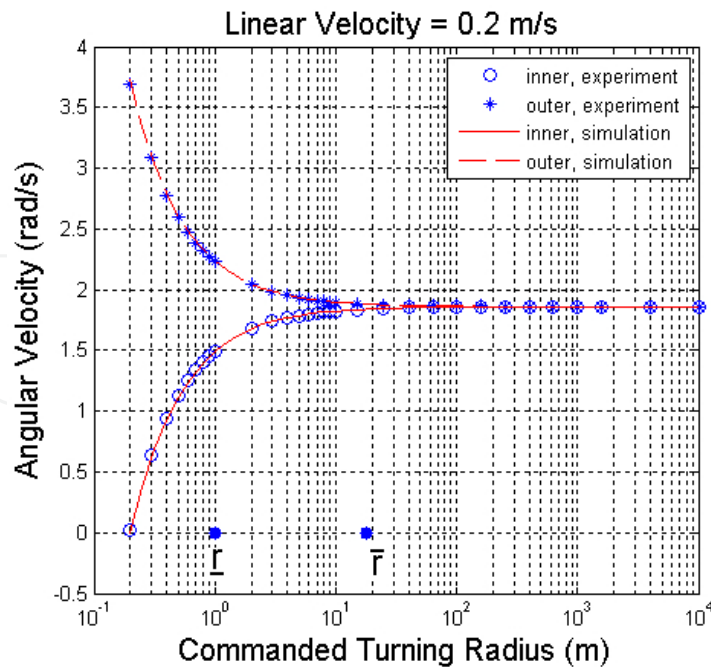


Fig. 14. Vehicle inner and outer wheel angular velocity comparison during steady-state CCW rotation for different commanded turning radii on the lab vinyl surface when the commanded linear velocity is 0.2 m/s.

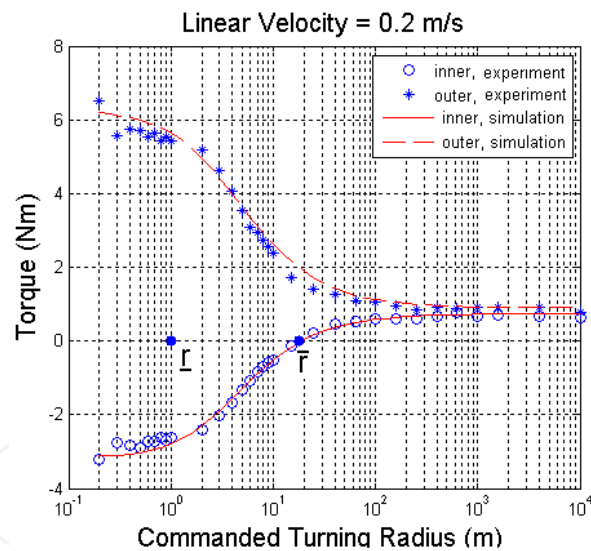


Fig. 15. Vehicle inner and outer wheel applied torque comparison corresponding to Fig. 14

approximately 58 w, which is above the 51 w power limitation, which means this velocity and radius combination cannot be achieved. However, the total power requirement in this case is also equal to 58 w. This power requirement is well below the 102 w limitation for the entire vehicle, showing the importance of estimating the power consumption of each individual motor. It is seen that as predicted by the power model for the outer wheel that this wheel was unable to achieve the desired vehicle due to the power limitation of the motor drive system. Fig. 18 compares the experimental, simulation and commanded angular velocity for the inner and outer wheels. Fig. 19 shows the experimental and simulation applied torques vs.

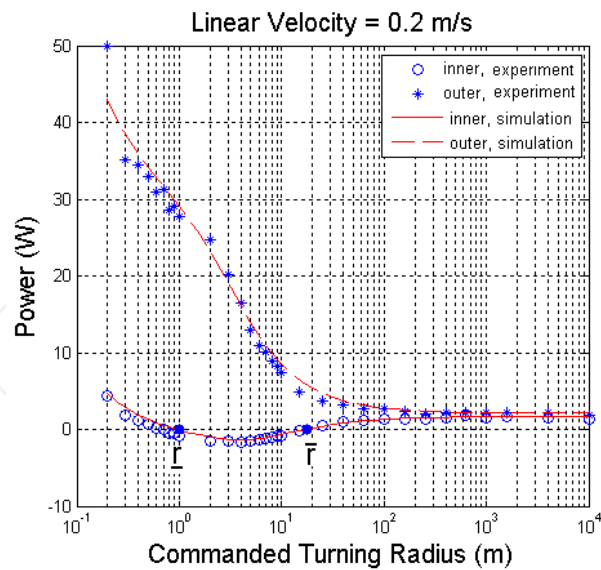


Fig. 16. Vehicle inner and outer wheel power comparison comparison corresponding to Fig. 14.

commanded radius and Fig. 20 shows the experimental and simulated power consumption vs. commanded radius.

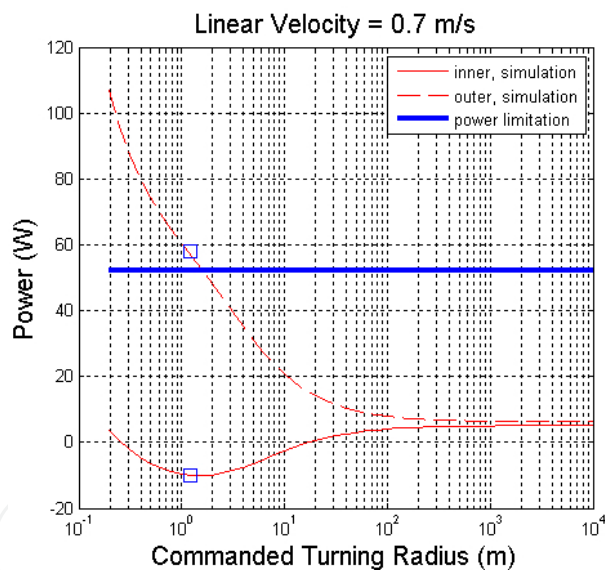


Fig. 17. Power limitation for each side of vehicle, and vehicle inner and outer wheel power prediction during steady-state CCW rotation for different commanded turning radii on the lab vinyl surface when the commanded linear velocity is 0.7 m/s

5.3 Curvilinear movement

In this subsection, the model is to be tested for general 2D curvilinear motion. The vehicle was commanded to move in lemniscate trajectory, which required it to have modest linear and angular accelerations. Fig. 21 shows one complete cycle lemniscate trajectory along with the partial lemniscate trajectory used in the experiment.

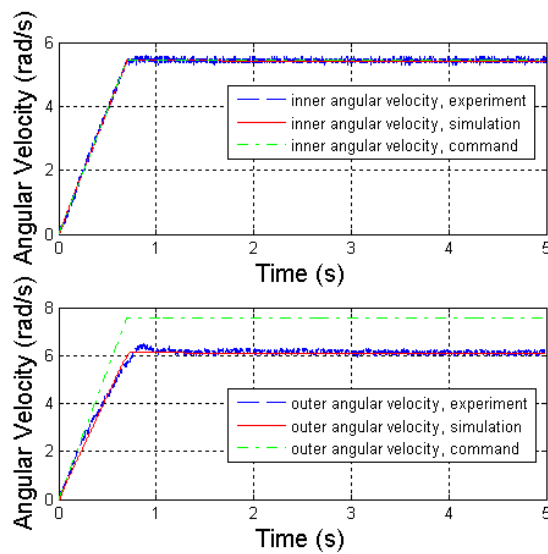


Fig. 18. Experiment, simulation and commanded angular velocity comparison for inner and outer wheels for 2D circular movement on the lab vinyl surface when the commanded radius is 1.2 m and the commanded linear velocity is 0.7 m/s.

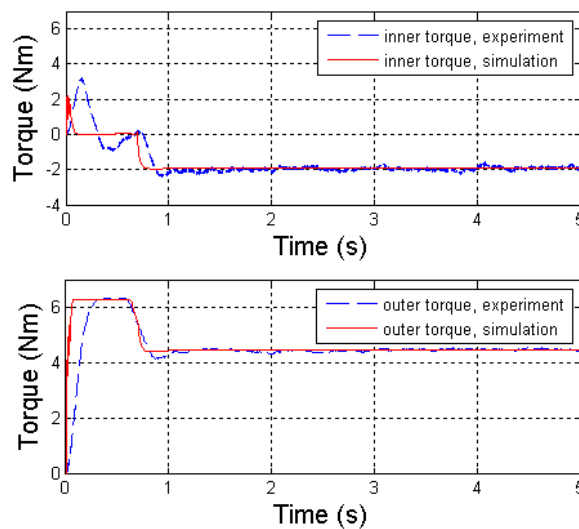


Fig. 19. Vehicle inner and outer wheels torque comparison corresponding to Fig. 18.

In Fig. 21, the lemniscate trajectory is governed by,

$$X(t) = \frac{9 \cos(\frac{t}{50})}{1 + \sin^2(\frac{t}{50})}, \tag{57}$$

$$Y(t) = \frac{27 \sin(\frac{t}{50}) \cos(\frac{t}{50})}{1 + \sin^2(\frac{t}{50})}, \tag{58}$$

where t is the time, and $(X(t), Y(t))$ is the position in global coordinates. The vehicle was first commanded to go straight with an acceleration of 1 m/s^2 to achieve the initial entering velocity 0.54 m/s of the lemniscate trajectory in Fig. 21 within 3 seconds. Then it was commanded to follow the desired trajectory in Fig. 21 with changing linear velocity and

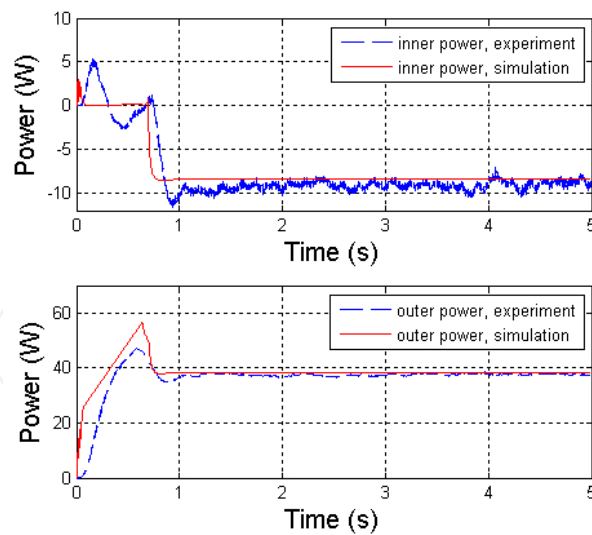


Fig. 20. Vehicle inner and outer wheels power comparison corresponding to Fig. 18.

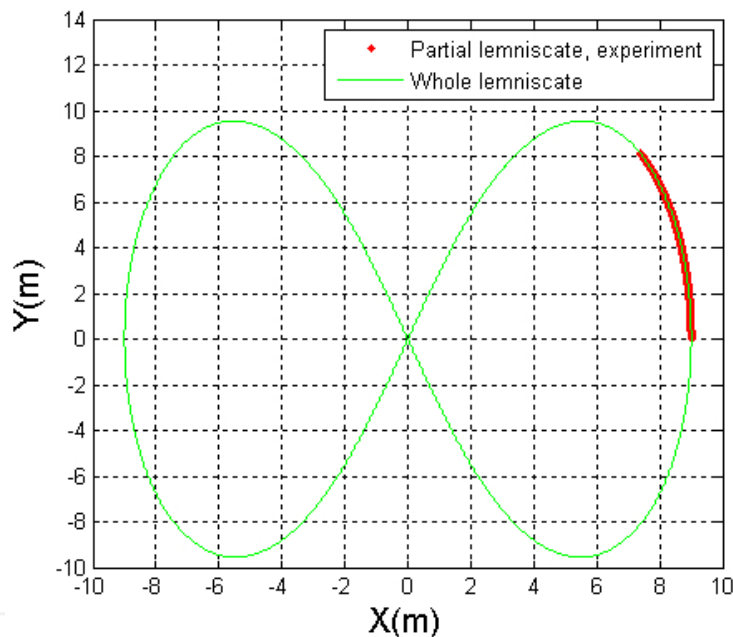


Fig. 21. Partial and whole lemniscate trajectories

turning radius for another 18 seconds. The linear acceleration changes in the range $[0 \ 0.02]$ m/s^2 .

Fig. 22, Fig. 23 and Fig. 24 show the experimental and simulation comparisons for the vehicle linear and angular velocity, the inner and outer wheel angular velocity, and the inner and outer wheel applied torque. Fig. 25 shows the corresponding power comparison for the inner and outer part of the vehicle. These results reveal that if the vehicle turns with continually changing linear and angular accelerations of limited magnitude, the dynamic models and power models are still capable of providing high fidelity predictions for both the inner and outer part of the vehicle. Fig. 25 also shows during the lemniscate traversal the inner motor gradually changes from consuming power to generating power while the outer motor always consumes power. The transition time for the inner motor can also be predicted from the motor power model (45).

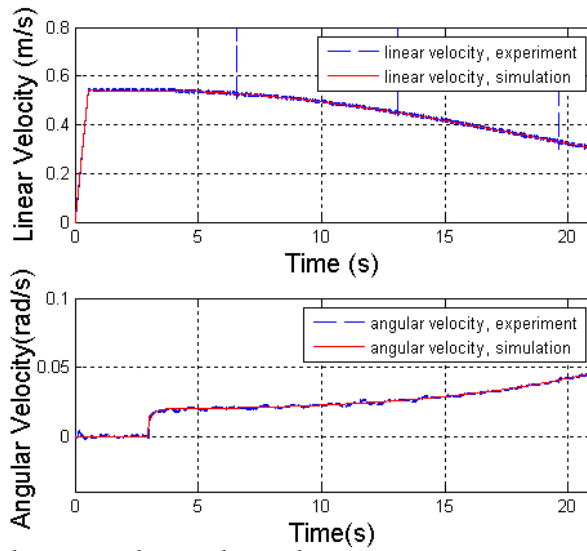


Fig. 22. Vehicle linear velocity and angular velocity comparison corresponding to lemniscate movement in Fig. 21

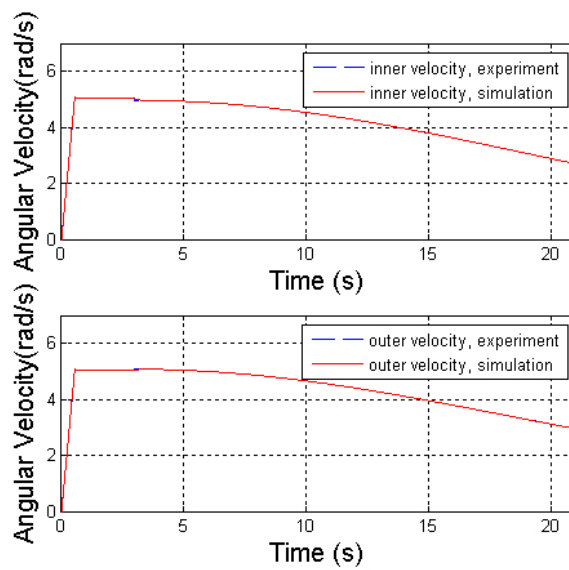


Fig. 23. Vehicle inner and outer wheel angular velocity comparison corresponding to lemniscate movement in Fig. 21

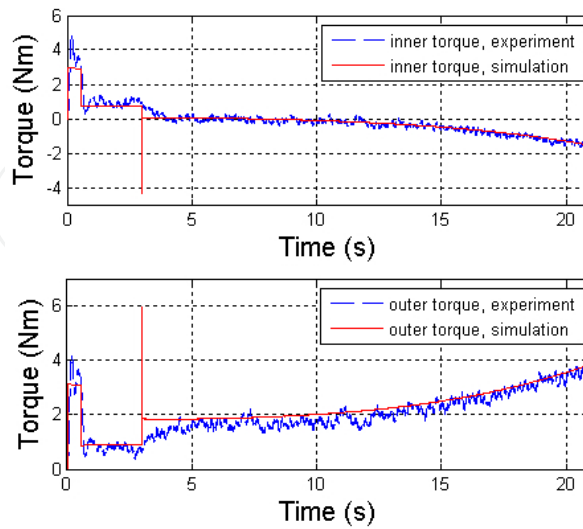


Fig. 24. Vehicle inner and outer wheel torque comparison corresponding to lemniscate movement in Fig. 21

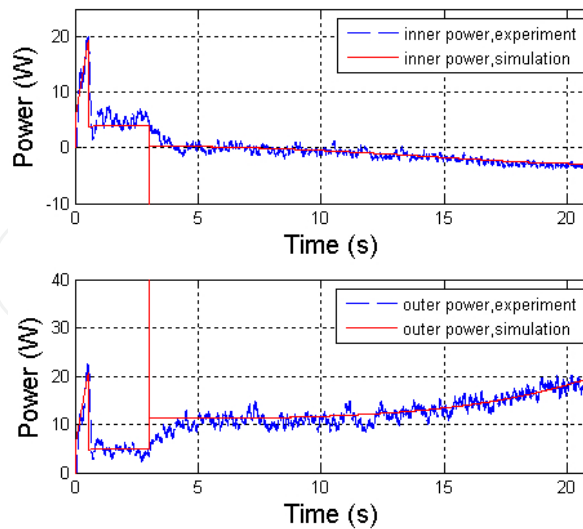


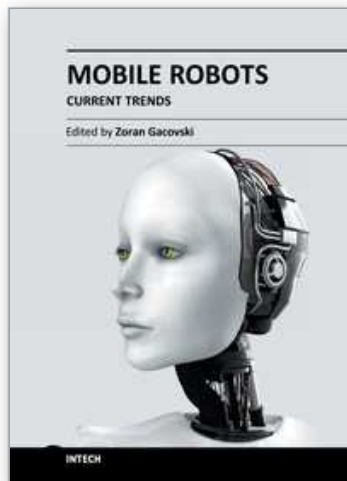
Fig. 25. Vehicle inner and outer wheel power comparison corresponding to lemniscate movement in Fig. 21

6. References

- Caracciolo, L., Luca, A. D. & Iannitti, S. (1999). Trajectory tracking control of a four-wheel differentially driven mobile robot, *Proceedings of the IEEE International Conference on Robotics and Automation*, Detroit, MI, pp. 2632–2638.
- Economou, J., Colyer, R., Tsourdos, A. & White, B. (2002). Fuzzy logic approaches for wheeled skid-steer vehicle, *Vehicular Technology Conference*, pp. 990–994.
- Endo, D., Okada, Y., Nagatani, K. & Yoshida, K. (2007). Path following control for tracked vehicles based slip-compensation odometry, *Proceedings of the IEEE International Conference on Intelligent Robots and Systems*, pp. 2871–2876.
- Golconda, S. (2005). *Steering control for a skid-steered autonomous ground vehicle at varying speed*, Master's thesis, University of Louisiana at Lafayette.
- Howard, T. M. & Kelly, A. (2007). Optimal rough terrain trajectory generation for wheeled mobile robots, *International Journal of Robotics Research* pp. 141–166.
- Kim, C. & Kim, B. K. (2007). Minimum-energy translational trajectory generation for differential-driven wheeled mobile robots, *Journal of Intelligent Robot System* pp. 367–383.
- Kozłowski, K. & Pazderski, D. (2004). Modeling and control of a 4-wheel skid-steering mobile robot, *International Journal of Mathematics and Computer Science* pp. 477–496.
- Mandow, A., Martíńez, J. L., Morales, J., Blanco, J.-L., Garcíła-Cerezo, A. & Gonzalez, J. (2007). Experimental kinematics for wheeled skid-steer mobile robots, *Proceedings of the International Conference on Intelligent Robots and Systems*, San Diego, CA, pp. 1222–1227.
- Martinez, J., Mandow, A., Morales, J., Pedraza, S. & Garcia-Cerezo, A. (2005). Approximating kinematics for tracked mobile robots, *International Journal of Robotics Research* pp. 867–878.
- Moosavian, S. A. A. & Kalantari, A. (2008). Experimental slip estimation for exact kinematics modeling and control of a tracked mobile robot, *Proceedings of the International Conference on Intelligent Robots and Systems*, Nice, France, pp. 95–100.
- Morales, J., Martinez, J. L., Mandow, A., Garcia-Cerezo, A., Gomez-Gabriel, J. & Pedraza, S. (2006). Power analysis for a skid-steered tracked mobile robot, *Proceedings of the IEEE International Conference on Mechatronics*, pp. 420–425.
- Morales, J., Martinez, J. L., Mandow, A., Garcia-Cerezo, A. J. & Pedraza, S. (2009). Power consumption modeling of skid-steer tracked mobile robots on rigid terrain, *IEEE Transactions on Robotics* pp. 1098–1108.
- Nagatani, K., Endo, D. & Yoshida, K. (2007). Improvement of the odometry accuracy of a crawler vehicle with consideration of slippage, *Proceedings of the International Conference on Robotics and Automation*, Rome, Italy, pp. 2752–2757.
- O. Chuy, J., E. Collins, J., Yu, W. & Ordonez, C. (2009). Power modeling of a skid steered wheeled robotic ground vehicle, *Proceedings of the IEEE International Conference on Robotics and Automation*, Kobe, Japan.
- Petrov, P., de Lafontaine, J., Bigras, P. & Tetreault, M. (2000). Lateral control of a skid-steering mining vehicle, *Proceedings of the International Conference on Intelligent Robots and Systems*, Takamatsu, Japan, pp. 1804–1809.
- Rizzoni, G. (2000). *Principles and Applications of Electrical Engineering*, McGraw-Hill.
- Shamah, B., Wagner, M. D., Moorehead, S., Teza, J., Wettergreen, D. & Whittaker, W. R. L. (2001). Steering and control of a passively articulated robot, *SPIE, Sensor Fusion and Decentralized Control in Robotic Systems IV*, Vol. 4571.

- Siegwart, R. & Nourbakhsh, I. R. (2005). *Introduction to Mobile Robotics*, MIT Press, Cambridge, MA.
- Song, X., Song, Z., Senevirante, L. & Althoefer, K. (2008). Optical flow-based slip and velocity estimation technique for unmanned skid-steered vehicles, pp. 101–106.
- Song, Z., Zweiri, Y. H. & Seneviratne, L. D. (2006). Non-linear observer for slip estimation of skid-steering vehicles, *Proceedings of the IEEE International Conference on Robotics and Automation*, Orlando, FL, pp. 1499–1504.
- Wang, H., Zhang, J., Yi, J., Song, D., Jayasuriya, S. & Liu, J. (2009). Modeling and motion stability analysis of skid-steered mobile robots, *Proceedings of the International Conference on Robotics and Automation*, Kobe, Japan, pp. 4112–4117.
- Wong, J. Y. (2001). *Theory of Ground Vehicle*, 3rd edn, John Wiley & Sons, Inc.
- Wong, J. Y. & Chiang, C. F. (2001). A general theory for skid steering of tracked vehicles on firm ground, *Proceedings of the Institution of Mechanical Engineers, Part D, Journal of Automotive Engineering* pp. 343–355.
- Yi, J., Song, D., Zhang, J. & Goodwin, Z. (2007). Adaptive trajectory tracking control of skid-steered mobile robots, *Proceedings of the IEEE International Conference on Robotics and Automation*, Roma, Italy, pp. 2605–2610.
- Yi, J., Zhang, J., Song, D. & Jayasuriya, S. (2007). IMU-based localization and slip estimation for skid-steered mobile robot, *Proceedings of the IEEE International Conference on Intelligent Robots and Systems*, San Diego, CA, pp. 2845–2849.
- Yu, W., Chuy, O., Collins, E. G. & Hollis, P. (2010). Analysis and experimental verification for dynamic modeling of a skid-steered wheeled vehicle, *IEEE Transactions on Robotics* pp. 440–453.
- Zhang, Y., Hong, D., Chung, J. H. & Velinsky, S. A. (1998). Dynamic model based robust tracking control of a differentially steered wheeled mobile robot, *Proceedings of The American Control Conference*, Philadelphia, PA, pp. 850–855.

IntechOpen



Mobile Robots - Current Trends

Edited by Dr. Zoran Gacovski

ISBN 978-953-307-716-1

Hard cover, 402 pages

Publisher InTech

Published online 26, October, 2011

Published in print edition October, 2011

This book consists of 18 chapters divided in four sections: Robots for Educational Purposes, Health-Care and Medical Robots, Hardware - State of the Art, and Localization and Navigation. In the first section, there are four chapters covering autonomous mobile robot Emmy III, KCLBOT - mobile nonholonomic robot, and general overview of educational mobile robots. In the second section, the following themes are covered: walking support robots, control system for wheelchairs, leg-wheel mechanism as a mobile platform, micro mobile robot for abdominal use, and the influence of the robot size in the psychological treatment. In the third section, there are chapters about I2C bus system, vertical displacement service robots, quadruped robots - kinematics and dynamics model and Epi.q (hybrid) robots. Finally, in the last section, the following topics are covered: skid-steered vehicles, robotic exploration (new place recognition), omnidirectional mobile robots, ball-wheel mobile robots, and planetary wheeled mobile robots.

How to reference

In order to correctly reference this scholarly work, feel free to copy and paste the following:

Wei Yu, Emmanuel Collins and Oscar Chuy (2011). Dynamic Modeling and Power Modeling of Robotic Skid-Steered Wheeled Vehicles, Mobile Robots - Current Trends, Dr. Zoran Gacovski (Ed.), ISBN: 978-953-307-716-1, InTech, Available from: <http://www.intechopen.com/books/mobile-robots-current-trends/dynamic-modeling-and-power-modeling-of-robotic-skid-steered-wheeled-vehicles>

INTECH
open science | open minds

InTech Europe

University Campus STeP Ri
Slavka Krautzeka 83/A
51000 Rijeka, Croatia
Phone: +385 (51) 770 447
Fax: +385 (51) 686 166
www.intechopen.com

InTech China

Unit 405, Office Block, Hotel Equatorial Shanghai
No.65, Yan An Road (West), Shanghai, 200040, China
中国上海市延安西路65号上海国际贵都大饭店办公楼405单元
Phone: +86-21-62489820
Fax: +86-21-62489821

© 2011 The Author(s). Licensee IntechOpen. This is an open access article distributed under the terms of the [Creative Commons Attribution 3.0 License](#), which permits unrestricted use, distribution, and reproduction in any medium, provided the original work is properly cited.

IntechOpen

IntechOpen